

# Edge-Diffraction Impulse Responses Near Specular-Zone and Shadow-Zone Boundaries

U. Peter Svensson

The Acoustics Group, Department of Electronics and Telecommunications, Norwegian University of Science and Technology, 7491 Trondheim, Norway

Paul T. Calamia\*

Department of Computer Science, Princeton University, Princeton, NJ 08540, USA

## Summary

Many methods for the computation of edge-diffraction impulse responses are based on the Biot-Tolstoy solution, an explicit, continuous-time expression for diffraction by an infinite wedge. This expression contains two singularities at the onset of the impulse response: one which is present for all source-receiver combinations, and a second which occurs only when a receiver moves across a specular-zone or shadow-zone boundary, *i.e.* a boundary where a geometrical-acoustics component has a discontinuity. For the calculation of discrete-time impulse responses, such a continuous-time analytical expression must be numerically integrated, and the singularities demand special attention. Svensson *et al.* [U. P. Svensson *et al.*, J. Acoust. Soc. Am. 106, 2331-2344 (1999)] presented an analytic, secondary-source model of edge diffraction based on the Biot-Tolstoy expression in which the first singularity was eliminated by reformulating the expression as an integral along the edge. In this paper, analytical approximations for the model presented by Svensson *et al.* are described which address the second type of singularity and thus allow for accurate numerical computations for receivers at or near zone boundaries. Implementation details are also provided, along with example calculations.

PACS no. 43.20.El, 43.20.Px

## 1. Introduction

Edge-diffraction impulse responses are often used as components in studies of acoustic scattering from objects with rigid, simple-shaped surfaces, *e.g.* in computer simulations of noise-barrier performance [1], radiation from loudspeakers [2], or room acoustics [3]. Many methods for the computation of edge-diffraction impulse responses are based on the explicit expression given by Biot and Tolstoy [4] for the diffraction of radiation from a point source by an infinite wedge. The Biot-Tolstoy solution was explored further by Medwin *et al.* [5, 6], who applied it to finite rather than infinite wedges, and interpreted the solution as a summation of secondary sources along an edge. Medwin's formulation is often referred to as the Biot-Tolstoy-Medwin (BTM) solution. Later, the BTM solution was developed into a line-integral formulation by Svensson *et al.* [7] that used analytical directivity functions for the secondary sources along the edge.

One difficulty associated with diffraction studies is that edge-diffraction impulse responses display two kinds of onset singularities. The first singularity is present for all source-receiver combinations, and the second occurs when the receiver moves across a specular-zone or shadow-zone boundary, *i.e.* a boundary where a geometrical-acoustics component has a discontinuity. For the calculation of discrete-time impulse responses, analytical diffraction expressions such as the BTM solution must be numerically integrated, and then these singularities demand special attention. Such integration is discussed specifically for the BTM solution in [8] and [9]. The formulation in [7] uses an analytic, secondary-source model of edge diffraction based on the BTM solution in which the first singularity has been eliminated by reformulating the expression as an integral along the edge. In this paper, an analytical approximation of the integrand in the impulse response expression in [7] is developed which allows for accurate diffraction calculations for receivers at or near zone boundaries.

Section 2 of this paper contains a review of the BTM edge-diffraction expressions, as well as those for the model derived in [7]. Section 3 describes analytical approximations for edge-diffraction impulse responses which are valid for receiver positions at or near zone boundaries. Section 4 presents implementation details, and section 5 provides results for several examples. Section 6 contains

---

Received 3 December 2004, revised April 2006,  
accepted 4 April 2006.

\* The second author is now on the faculty of the Program in Architectural Acoustics in the School of Architecture at Rensselaer Polytechnic Institute, Troy, NY USA.

conclusions and discussions of future work. Appendices A1 and A2 contain mathematical derivations of the approximations in section 3, as well as several intermediate quantities needed for the calculations.

## 2. Edge-diffraction impulse responses

### 2.1. The BTM formulation

Consider a rigid wedge, with a point source  $S$  and a receiver  $R$  whose positions are given with cylindrical coordinates  $(r_S, \theta_S, z_S)$  and  $(r_R, \theta_R, z_R)$ , respectively, as shown in Figure 1. The source signal is defined as  $q(t) = \rho_0 A(t)/4\pi$ , where  $\rho_0$  is the density of air and  $A(t)$  is the volume acceleration of the point source. Such a source signal implies that the free-field impulse response of the source is  $h(\tau) = \delta(\tau - d/c)/d$  where  $d$  is the distance from the source to the receiver and  $c$  is the speed of sound, and sound pressure can be calculated through the convolution integral

$$p(t) = \int_0^\infty h(\tau)q(t - \tau) d\tau. \quad (1)$$

The edge-diffraction impulse response (IR),  $h_{diff}(\tau)$ , then can be formulated for a rigid wedge<sup>1</sup> of infinite extent as suggested by Clay and Kinney [8] or Medwin *et al.* [6], as based on the Biot-Tolstoy solution [4],

$$h_{diff}(\tau) = -\frac{c\nu}{2\pi r_S r_R} \sum_{i=1}^4 \frac{\beta_i(\tau)}{\sinh[\eta(\tau)]} H(\tau - \tau_0), \quad (2)$$

where  $\nu = \pi/\theta_W$  is the wedge index,  $\theta_W$  is the open angle of the wedge,  $H(\tau - \tau_0)$  is a Heaviside unit step function, and  $\tau_0$  is the onset time of the diffraction IR, given by  $\tau_0 = R_0/c$ . The distance

$$R_0 = \sqrt{(r_S + r_R)^2 + (z_R - z_S)^2} \quad (3)$$

is the shortest distance from the source to the receiver via a point on the edge. This point is called the apex point. The functions  $\beta_i(\tau)$  are

$$\beta_i(\tau) = \frac{\sin(\nu\varphi_i)}{\cosh[\nu\eta(\tau)] - \cos(\nu\varphi_i)}, \quad (4)$$

where the angles  $\varphi_i$  are

$$\begin{aligned} \varphi_1 &= \pi + \theta_S + \theta_R, & \varphi_2 &= \pi + \theta_S - \theta_R, \\ \varphi_3 &= \pi - \theta_S + \theta_R, & \varphi_4 &= \pi - \theta_S - \theta_R, \end{aligned} \quad (5)$$

and the auxiliary function  $\eta(\tau)$  is

$$\eta(\tau) = \cosh^{-1} \left\{ \frac{c^2\tau^2 - [r_S^2 + r_R^2 + (z_R - z_S)^2]}{2r_S r_R} \right\}. \quad (6)$$

<sup>1</sup> The solution for a pressure-release wedge or a wedge with both rigid and pressure-release faces can be expressed with modifications to the summation of the  $\beta_i$  terms. For details see [4] or [7].

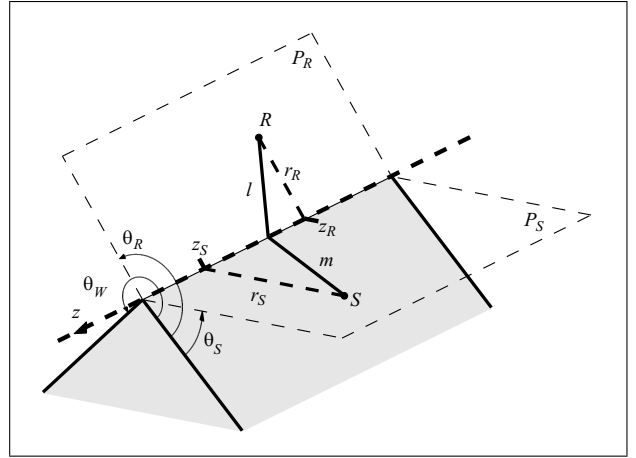


Figure 1. Wedge geometry and coordinate system. Locations are specified with cylindrical coordinates  $(r, \theta, z)$  where  $r$  is the radial distance from the edge,  $\theta$  is measured from one of the two wedge faces, and the  $z$ -axis is aligned with the edge (crest) of the wedge. For a given point on the edge, the distances  $m$  and  $l$  are measured in the virtual half-planes  $P_S$  and  $P_R$ , respectively, where  $P_S$  is the half-plane which contains the edge and the source  $S$ , and  $P_R$  is the half-plane which contains the edge and the receiver  $R$ . The path from  $S$  to  $R$  shown goes through the apex point on the edge.

Equation (2) is an explicit, exact expression for an infinite wedge. However, in most computational applications, a discrete-time representation,  $h_{diff}(n)$ , is needed, and the standard technique is to area-sample the continuous-time expression. Such an area-sampling corresponds to the integration of the analytic expression over a time range which is  $\pm 0.5/f_S$  around each sample instant,

$$h_{diff}(n) = \int_{(n-0.5)/f_S}^{(n+0.5)/f_S} h_{diff}(\tau) d\tau, \quad (7)$$

where  $n$  is the sample index and  $f_S$  is the sampling frequency. In [8], numerical aspects of this integration are studied in detail, and the two singularities of equation (2) are noted to be of special importance. The first singularity is caused by the function  $\sinh[\eta(\tau)]$  which equals zero for the onset of the diffraction IR at  $\tau = \tau_0$ , and occurs for all source-receiver combinations. The second singularity occurs when the denominator of one or two of the  $\beta_i$  terms takes the value zero. This singularity also happens at the IR onset, but only for specific source-receiver combinations such that the receiver is on a zone boundary (see Figure 2). Both singularities require some care for the numerical integration technique.

### 2.2. The analytic edge-source model

An alternative formulation for the edge diffraction IR was presented in [7], in which the explicit solution of equation (2) was replaced by a line integral formulation along the edge which eliminated the first singularity. Using the  $z$ -

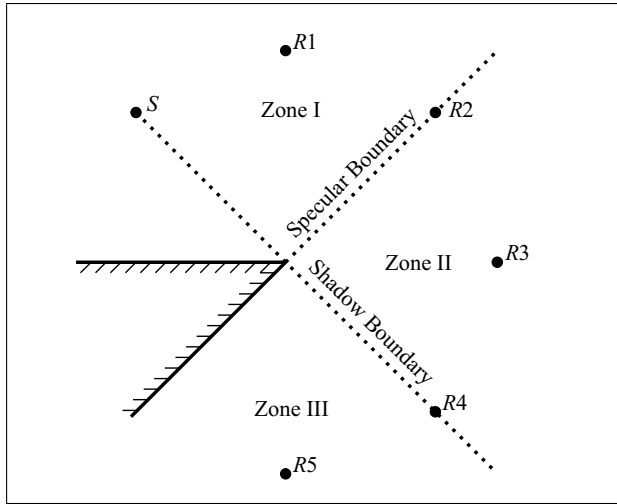


Figure 2. Zones defined by the geometrical-acoustics components for the given wedge and source position. A receiver in Zone I (e.g.  $R1$ ) will experience the direct sound and a specular reflection. A receiver in Zone II (e.g.  $R3$ ) will experience only the direct sound. A receiver in Zone III (e.g.  $R5$ ) will experience neither. Sound diffracted from the edge will propagate into all zones. Receivers  $R2$  and  $R4$  (where  $\theta_R = \pi \mp \theta_S$ ) are on the zone boundaries, and are subject to the diffraction singularities described in sections 2 and 3.

coordinate as the integration variable, the continuous-time IR is given by the expression

$$h_{diff}(\tau) = -\frac{v}{4\pi} \sum_{i=1}^4 \int_{z_1}^{z_2} \delta\left(\tau - \frac{m+l}{c}\right) \frac{\beta_i}{ml} dz, \quad (8)$$

where  $m$  and  $l$  are the distances from the source to the edge point and the receiver to the edge point, respectively, as seen in Figure 1, and  $\delta$  is the Dirac delta function. The functions  $\beta_i$  are now interpreted as edge-source directivity functions, using an alternative formulation for  $\cosh(v\eta)$  which is a function of  $z$  (described in Appendix A1). For a finite wedge, the total edge-diffraction solution is obtained by using the  $z$ -coordinate values of the edge end-points for the integration limits  $z_1$  and  $z_2$ .

The transition from the continuous-time expression in equation (8) to a discrete-time formulation using the area-sampling in equation (7) is accomplished by setting the integration limits  $z_1$  and  $z_2$  for the  $n$ th sample to points along the edge that correspond to the travel times  $(n-0.5)/f_S$  and  $(n+0.5)/f_S$ , respectively, thus

$$h_{diff}(n) = -\frac{v}{4\pi} \sum_{i=1}^4 \int_{z_{n,1}}^{z_{n,2}} \frac{\beta_i}{ml} dz. \quad (9)$$

The calculation of such integration limits is described in Appendix A2. As discussed in [5] and [6], there can be two points on an edge, one on each side of the apex point, that correspond to a given travel time  $\tau$ . Therefore, there may be two short segments that contribute to the  $n$ th sample, *i.e.* two valid values for both  $z_{n,1}$  and  $z_{n,2}$ . Such segments correspond to portions of the edge which lie between intersections of the edge and two confocal ellipsoids whose foci are the source and receiver locations, and

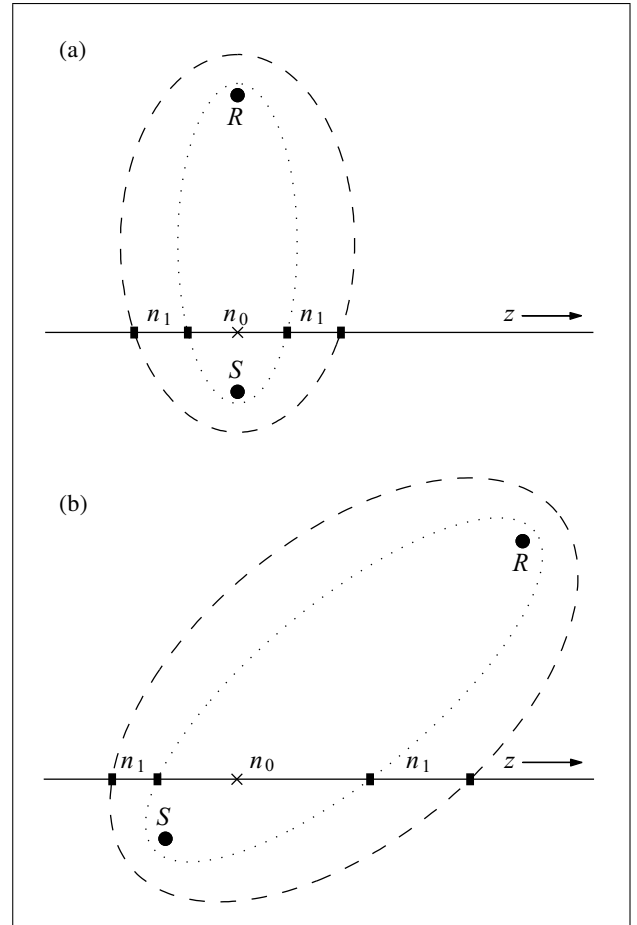


Figure 3. Unfolded 2D view of segments contributing to the first two samples of an edge-diffraction IR for (a) symmetric and (b) asymmetric source/receiver geometries. In both cases, the segment of the edge within the dotted ellipse contributes to the first sample of the edge-diffraction IR ( $n_0$ ), and the two segments between the dotted and dashed ellipses to the second sample ( $n_1$ ). The apex point is marked with an 'x' in both cases. For the asymmetric case, the two segments marked  $n_1$  are of different lengths, but contribute equally to the second sample of the edge-diffraction IR.

whose axes lengths are determined by the travel distances  $c(n \pm 0.5)/f_S$ . 2D examples of this are shown in Figure 3. Both segments must be taken into account for the correct solution. Further discussion of the integration limits can be found in section 3.3.

### 3. Analytical approximation

#### 3.1. Overview

It was argued in [7] that the integrand  $\beta_i/ml$  in equations (8) and (9) is well behaved because the singularity due to the  $1/\sinh[\eta(\tau)]$  term has been eliminated, and in general the well-behaved integrand makes numerical integration of equation (9) fast and accurate. However, the singularity due to the  $\beta_i$  terms still occurs for receivers as they cross the zone boundaries. As indicated earlier, this singularity occurs when the terms  $\cosh(v\eta)$  and  $\cos(v\varphi_i)$  in

equation (4) both take the value 1 for certain combinations of  $\theta_S$  and  $\theta_R$ .<sup>2</sup> The singularity in the diffraction component is necessary to compensate for the discontinuity in the geometrical-acoustics component and thus maintain a continuous sound field across the zone boundary. The singular behavior of the integrand occurs for  $z$ -values around the apex point, and this suggests an approach with an analytic approximation of the integrand which is valid and accurate around the apex point. Since the apex point is contained within the segment of the edge that contributes to the first edge-diffraction IR sample, the following approximations have been developed specifically for this first sample.

### 3.2. Approximating the integrand

Given an edge, source, and receiver, the  $z$ -coordinate of the apex point is

$$z_a = \frac{z_R r_S + z_S r_R}{r_S + r_R}, \quad (10)$$

and an approximation of the integrand  $\beta_i/ml$  near the apex point can be made using a  $z$ -coordinate measured relative to  $z_a$ ,

$$z_{rel} = z - z_a. \quad (11)$$

Following the steps in Appendix A1, approximations for  $\cosh(v\eta)$  and  $ml$  can be derived for small values of  $z_{rel}$ :

$$\cosh(v\eta) \approx 1 + v^2 \frac{(1 + \rho)^4}{2\rho^2 R_0^2} z_{rel}^2, \quad (12)$$

and

$$ml \approx \frac{R_0^2 \rho}{(1 + \rho)^2} + \frac{\cos \psi R_0 (\rho - 1)}{\rho + 1} z_{rel} + \frac{\sin^2 \psi (1 + \rho)^2 - 2\rho}{2\rho} z_{rel}^2, \quad (13)$$

where the dimensionless quantity  $\rho$  is defined as

$$\rho = \frac{r_R}{r_S}, \quad (14)$$

and the angle  $\psi$ , shown in Figure 4, is defined such that

$$\sin \psi = \frac{r_S + r_R}{R_0}, \quad \cos \psi = \frac{z_R - z_S}{R_0}. \quad (15)$$

Using equations (12) – (15), the integrand  $\beta_i/ml$  can be approximated as

$$\frac{\beta_i}{ml} \approx B_0 \cdot \frac{1}{z_{rel}^2 + B_1} \cdot \frac{1}{z_{rel}^2 + B_2 z_{rel} + B_3}, \quad (16)$$

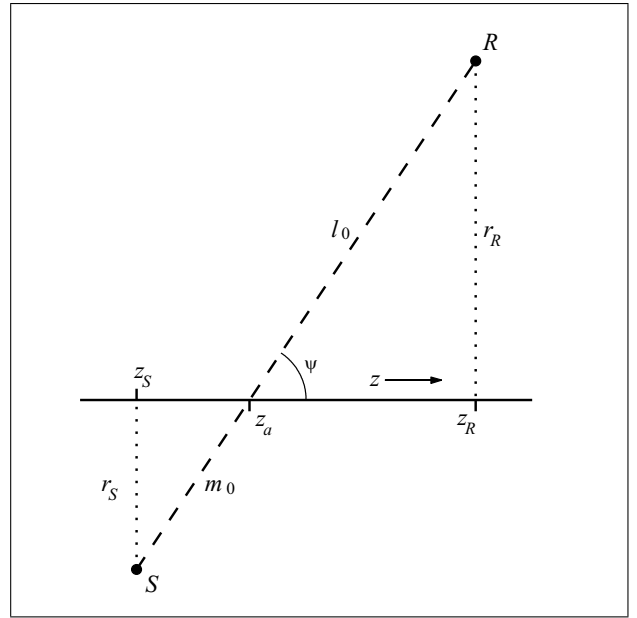


Figure 4. Unfolded 2D view of a wedge, source, and receiver showing the angle  $\psi$ . For the expressions in equation (15), note that  $R_0 = m_0 + l_0$ .

where

$$\begin{aligned} B_0 &= \frac{4R_0^2 \rho^3 \sin(v\varphi_i)}{v^2(1 + \rho)^4 [(1 + \rho)^2 \sin^2 \psi - 2\rho]}, \\ B_1 &= \frac{4R_0^2 \rho^2 \sin^2(\frac{v\varphi_i}{2})}{v^2(1 + \rho)^4}, \\ B_2 &= -\frac{2R_0(1 - \rho)\rho \cos \psi}{(1 + \rho) [(1 + \rho)^2 \sin^2 \psi - 2\rho]}, \\ B_3 &= \frac{2R_0^2 \rho^2}{(1 + \rho)^2 [(1 + \rho)^2 \sin^2 \psi - 2\rho]}. \end{aligned} \quad (17)$$

Note that only  $B_0$  and  $B_1$  are functions of  $\varphi_i$ . The finite integral in equation (9) can be solved analytically when the integrand is given by equation (16), and the solution is presented in sections 3.4 and 3.5, treating the symmetrical ( $\rho = 1$  or  $\psi = \pi/2$ ) and asymmetrical cases separately. The solution for the symmetrical case was introduced in a slightly modified form in [10].

### 3.3. Limits of integration

As mentioned above, the analytical approximation is needed only for the first sample of the edge-diffraction IR,  $h(n_0)$ , because it is only this sample that is affected by the singularity in the original integrand. Therefore, the limits of integration for the approximation will typically be the  $z$ -values which delineate the portion of the edge that contributes to the first sample of the IR. Using  $z$ -coordinates relative to the apex point, one of these values will be negative ( $z_0^-$ ) and the other positive ( $z_0^+$ ) (as can be seen in Figure 3), and thus for the first sample equation (9) can be

<sup>2</sup> Since  $\cosh(v\eta) \geq 1$  and  $\cos(v\varphi_i) \leq 1$ , the singularity can occur only when  $\cosh(v\eta) = \cos(v\varphi_i) = 1$ .

written

$$\begin{aligned} h(n_0) &= -\frac{\nu}{4\pi} \sum_{i=1}^4 \int_{z_0^-}^{z_0^+} \frac{\beta_i}{ml} dz \\ &= -\frac{\nu}{4\pi} \left( \sum_{i=1}^4 \int_{z_0^-}^0 \frac{\beta_i}{ml} dz + \sum_{i=1}^4 \int_0^{z_0^+} \frac{\beta_i}{ml} dz \right). \end{aligned} \quad (18)$$

It was shown in [7] that two segments on opposite sides of the apex point which contribute to the same sample do so equally, therefore

$$\sum_{i=1}^4 \int_{z_0^-}^0 \frac{\beta_i}{ml} dz = \sum_{i=1}^4 \int_0^{z_0^+} \frac{\beta_i}{ml} dz. \quad (19)$$

This equality holds even for the asymmetrical case when  $|z_0^-| \neq |z_0^+|$  (see Figure 3b). Equation (18) can now be restated

$$h(n_0) = -\frac{\nu}{2\pi} \sum_{i=1}^4 \int_0^{z_0^+} \frac{\beta_i}{ml} dz. \quad (20)$$

In the sections that follow, approximations are presented for the  $i$ th term of the summation in equation (20), written as one-sided integrals with a lower limit of 0 and an upper limit which is positive. Cases for which this form is not appropriate, or for which  $z_0^+$  is not an appropriate choice for the upper limit of integration, are discussed in section 4.2.

### 3.4. Approximation for the symmetrical case

For a symmetrical geometry, either  $z_S = z_R$ , *i.e.*  $\psi = \pi/2$ , or  $r_S = r_R$ , *i.e.*  $\rho = 1$ , and in both cases  $B_2 = 0$  in equation (16). The integral which gives the first sample of the discrete-time IR,  $h(n_0)$ , is the sum of the four IR terms denoted  $h_i(n_0)$ , and the  $i$ th term is

$$h_i(n_0) \approx -\frac{\nu}{2\pi} \cdot \frac{B_0}{B_3 - B_1} \cdot \int_0^{z_{range}} \left( \frac{1}{z_{rel}^2 + B_1} - \frac{1}{z_{rel}^2 + B_3} \right) dz_{rel}. \quad (21)$$

where  $z_{range}$  is typically  $z_0^+$ , the  $z$ -coordinate of the point on the edge corresponding to  $\tau = (n_0 + 0.5)/f_S$ , as described in section 3.3. The result of this integration is

$$h_i(n_0) \approx -\frac{\nu}{2\pi} \cdot \frac{B_0}{B_3 - B_1} \cdot \left[ \frac{1}{\sqrt{B_1}} \arctan \left( \frac{z_{range}}{\sqrt{B_1}} \right) - \frac{1}{\sqrt{B_3}} \arctan \left( \frac{z_{range}}{\sqrt{B_3}} \right) \right]. \quad (22)$$

A special case of the symmetrical situation occurs when  $\rho = 1$  and  $\psi = \pi/4$ . The integrand  $\beta_i/ml$  then simplifies to

$$\frac{\beta_i}{ml} \approx B_4 \frac{1}{z_{rel}^2 + B_1}, \quad (23)$$

where

$$B_4 = \frac{B_0}{B_3} = \frac{\sin(\nu\varphi_i)}{2\nu^2}. \quad (24)$$

The result of the integration in this case is

$$h_i(n_0) \approx -\frac{\nu}{2\pi} \cdot \frac{B_4}{\sqrt{B_1}} \cdot \arctan \left( \frac{z_{range}}{\sqrt{B_1}} \right). \quad (25)$$

### 3.5. Approximation for the asymmetrical case

For the general, asymmetrical case, the integral form for the  $i$ th term of the first sample of the diffraction IR is

$$\begin{aligned} h_i(n_0) &\approx \frac{\nu}{2\pi} \cdot \frac{B_0 B_2}{B_1 B_2^2 + (B_1 - B_3)^2} \\ &\cdot \int_0^{z_{range}} \left[ \frac{z_{rel} + (B_1 - B_3)/B_2}{z_{rel}^2 + B_1} - \frac{z_{rel} + (B_1 - B_3 + B_2^2)/B_2}{z_{rel}^2 + B_2 z_{rel} + B_3} \right] dz_{rel}. \end{aligned} \quad (26)$$

The result of this integration is

$$\begin{aligned} h_i(n_0) &\approx \frac{\nu}{2\pi} \cdot \frac{B_0 B_2}{B_1 B_2^2 + (B_1 - B_3)^2} \\ &\cdot \left[ \frac{1}{2} \ln \left| \frac{B_3 (z_{range}^2 + B_1)}{B_1 (z_{range}^2 + B_2 z_{range} + B_3)} \right| \right. \\ &\left. + \frac{B_1 - B_3}{\sqrt{B_1 B_2}} \arctan \left( \frac{z_{range}}{\sqrt{B_1}} \right) \right. \\ &\left. + \frac{2(B_3 - B_1) - B_2^2 F}{2B_2} \right], \end{aligned} \quad (27)$$

where  $F$  can take one of four forms depending on the quantity

$$q = 4B_3 - B_2^2. \quad (28)$$

For  $q < 0$  and finite, form I should be used, where

$$F_I = \frac{1}{\sqrt{-q}} \ln \left( \left| \frac{2z_{range} + B_2 - \sqrt{-q} B_2 + \sqrt{-q}}{2z_{range} + B_2 + \sqrt{-q} B_2 - \sqrt{-q}} \right| \right), \quad (29)$$

and for  $q > 0$  and finite, form II should be used, where

$$F_{II} = \frac{2}{\sqrt{q}} \left( \arctan \frac{2z_{range} + B_2}{\sqrt{q}} - \arctan \frac{B_2}{\sqrt{q}} \right). \quad (30)$$

When  $q = 0$ , the third form is

$$F_{III} = \frac{4z_{range}}{B_2(2z_{range} + B_2)}. \quad (31)$$

The fourth form,

$$F_{IV} = 0, \quad (32)$$

is used when the denominator of  $q$  goes to zero. When  $q$  is written

$$q = \frac{4R_0^2 \rho^2 [2(1 + \rho^2) - \cos^2 \psi (1 + 6\rho + \rho^2)]}{(1 + \rho)^2 [(1 + \rho)^2 \sin^2 \psi - 2\rho]}, \quad (33)$$

it is clear that the denominator will be zero when

$$\sin^2 \psi = \frac{2\rho}{(1 + \rho)^2}, \quad (34)$$

or, equivalently, when

$$\rho = \cot^2 \psi \cdot \left(1 \pm \sqrt{1 - \tan^4 \psi}\right). \quad (35)$$

$F_{IV}$  can be used directly in equation (27); however an alternative formulation of equation (26) is numerically more suitable in this case,

$$h_i(n_0) \approx \frac{\nu}{2\pi} \frac{B_5}{B_1 + B_6^2} \int_0^{z_{range}} \left( \frac{z_{rel} - B_6}{z_{rel}^2 + B_1} - \frac{1}{z_{rel} + B_6} \right) dz_{rel}. \quad (36)$$

The result of this integration is

$$h_i(n_0) \approx \frac{\nu}{2\pi} \frac{B_5}{B_1 + B_6^2} \left[ \frac{1}{2} \ln \left| \frac{B_6^2 (z_{range}^2 + B_1)}{B_1 (z_{range} + B_6)^2} \right| - \frac{B_6}{\sqrt{B_1}} \arctan \left( \frac{z_{range}}{\sqrt{B_1}} \right) \right], \quad (37)$$

where

$$B_5 = \frac{B_0}{B_2} = -\frac{2R_0 \rho^2 \sin(\nu \varphi_i)}{\nu^2 (1 + \rho)^3 (1 - \rho) \cos \psi}, \quad (38)$$

and

$$B_6 = \frac{B_3}{B_2} = -\frac{R_0 \rho}{(1 - \rho^2) \cos \psi}. \quad (39)$$

There is no risk that the denominator of  $B_5$  or  $B_6$  will take the value zero, since that can happen only for the symmetrical cases  $\rho = 1$  and  $\psi = \pi/2$  which have been addressed separately.

### 3.6. Limit value for the IR approximations

To address the singularity normally seen for receivers at or near zone boundaries, the impulse-response expressions from the preceding sections must be evaluated as the angle  $\varphi_i$  approaches 0. The approach must be considered from both sides of the boundary, *i.e.* as  $\varphi_i \rightarrow 0^+$  and  $\varphi_i \rightarrow 0^-$ . For equations (22), (25), (27), and (37), a finite value will result, and the limiting case of the receiver being close to a zone boundary is

$$\lim_{\varphi_i \rightarrow 0^\pm} h_i(n_0) = \mp \frac{1}{2R_0}. \quad (40)$$

This is an interesting limit value since it shows that as the receiver approaches a zone boundary, the diffraction IR will tend toward a pulse (since the IR value in the first time sample will dominate the values in the following samples) with an amplitude which is half that of the geometrical component associated with that boundary. On the “illuminated” side of the boundary, *i.e.* where the direct sound or specular reflection reaches the receiver, the geometrical component and the diffraction IR will have opposite polarities (with amplitudes of  $\frac{1}{R_0}$  and  $\frac{-1}{2R_0}$ , respectively), and thus at the boundary will fuse into a single pulse with amplitude  $\frac{1}{2R_0}$ . Just beyond the zone boundary, the diffraction IR maintains the amplitude of  $\frac{1}{2R_0}$  and the geometrical-acoustics component disappears, and thus the total sound field is continuous across the boundary. This limit value is consistent with the one reported by Clay *et al.* in [11], although Clay and Kinney suggest in [8] that the limit is in fact zero. Equation (40) is also in agreement with [12] in which the author shows that the *change* in the diffracted field as a receiver crosses the shadow boundary is in the limit equal to the amplitude of the direct sound just prior to its disappearance.

A second interesting characteristic of this limit is that it is independent of both the wedge angle  $\theta_W$  and the edge length, suggesting that for a receiver near a zone boundary the diffraction from all wedges with the same orientation is the same. However, the remainder of the diffraction IR (non-singular  $h_i(n_0)$  terms as well as  $h(n_1)$ ,  $h(n_2)$ , etc.) does vary with  $\theta_W$  and its duration is a function of the edge length, and thus this independence from the wedge properties is observed in the diffraction IR only at asymptotically high frequencies. The low-frequency limit is given by the integral of the entire edge-diffraction IR, including the initial pulse as well as the weaker contributions of the later sample times. See section 5 and Figure 8 for further details. The non-singular terms and later sample values vary smoothly across zone boundaries, and thus do not disturb the continuity of the overall sound field across the boundaries.

The high-frequency independence from  $\theta_W$  may seem to conflict with the fact that edges with certain wedge angles do not produce a diffracted wave. For example, consider an edge with  $\theta_W = \pi$ , *i.e.* an edge between two coplanar surfaces. The limit value of  $\pm \frac{1}{2R_0}$  is still valid, but in this case it applies to *two* terms (either  $h_1(n_0)$  and  $h_4(n_0)$  or  $h_2(n_0)$  and  $h_3(n_0)$ ) with opposite polarities which sum to zero and thus give the expected result. This case is studied further in section 5.

This limit value suggests three possible interpretations for the values of the diffraction IR and the geometrical component when the receiver is located *exactly* on a zone boundary. To maintain continuity of the sound field, the geometrical component and diffraction IR can be assigned amplitudes  $\frac{1}{R_0}$  and  $\frac{-1}{2R_0}$ ,  $\frac{1}{2R_0}$  and 0, or 0 and  $\frac{1}{2R_0}$  respectively for such cases. It may be that this choice of interpretation lead to the apparently conflicting results in [8] and [11]. Li and Clay [13] provide experimental evidence that the first interpretation is the correct one, although it

is not clear how precisely one can place a receiver on a zone boundary in an experimental setup. For the results presented in section 5 below, the second interpretation has been used.

## 4. Implementation details

Implementation of the relations derived in the previous section is generally straightforward, although there are a few aspects which require special attention. These include sub-dividing edges and choosing an appropriate value for  $z_{range}$ .

### 4.1. Edge subdivision

A discrete-time edge-diffraction IR can be calculated once the edge is subdivided into small segments. One possible method is to subdivide the edge such that each segment contributes to exactly one sample of the impulse response as in equation (9). Calculations of the appropriate segment boundaries for this method are described in Appendix A2, and a partial example of such a subdivision is shown in Figure 3. For the element that contributes to the first sample of the discrete-time IR (*i.e.* the element that contains the apex point), the expression in equation (22), (25), (27), or (37) should be used to calculate the contribution. For all other edge elements, a simple numerical implementation of equation (9) can be used with a standard numerical integration technique. This method of subdivision has the advantage of being most easily integrated with the approximations derived in section 3 since the segment that contains the apex point is given explicitly. However, the segment boundaries are dependent on the source and receiver positions, and thus must be recalculated if either is moved.

As discussed in [7], an alternative method involves dividing each edge into equally sized elements of length  $\Delta z$ . If this length is chosen such that  $\Delta z < c/2f_S$  (where  $c$  is the speed of sound and  $f_S$  is the sampling frequency), the contribution from each element will not spread over more than two samples. Such a method is simple to implement, and the subdivisions are independent of the source and receiver positions and thus can be re-used if the source and/or receiver is moved. However, such elements must be classified as contributing to either one or two samples during processing, and the contribution must be distributed accordingly. This classification does change when the source and/or receiver is moved. Elements also must be tested for inclusion of the apex point since this subdivision method does not provide that information directly. Further details on edge-subdivision strategies can be found in [14].

### 4.2. Appropriate value of $z_{range}$

Calculations using equations (22), (25), (27), and (37) require an appropriate choice of the value  $z_{range}$ , the upper limit of integration for the approximations. Since  $z_{range}$  must be positive (per section 3.3), a simple, initial choice is  $z_0^+$ , the positive-valued end-point of the edge segment

that contributes to the first IR sample  $h(n_0)$ . However, certain conditions must be satisfied in order for the use of this value in the approximation to yield an accurate result. The validity of  $z_0^+$  is most easily addressed for two separate cases.

The first case involves an edge which extends beyond  $z_0^-$  in the negative direction and beyond  $z_0^+$  in the positive direction, *i.e.* the entire segment that contributes to the first sample of the IR is contained within the edge.<sup>3</sup> In this case, it is sufficient to confirm that  $z_0^+$  is small compared with  $m_0$  and  $l_0$  (see Appendix A1). If so, then  $z_0^+$  is an appropriate value for  $z_{range}$ . If not, a smaller value for  $z_{range}$  must be chosen, *e.g.*  $0.05 \times \min(m_0, l_0)$ . When using a value smaller than  $z_0^+$  for  $z_{range}$ , the remainder of the contribution to the first sample of the diffraction IR can be calculated using numerical integration of equation (9), setting  $z_{n,1} = z_{range}$  and  $z_{n,2} = z_0^+$ . The result of this numerical integration must be doubled to account for the contributions from both sides of the apex point.

The second case involves an edge for which one or both of the edge end-points lie within the interval  $(z_0^-, z_0^+)$ , *i.e.* only part of the segment that would otherwise contribute to the first sample of the IR is actually contained within the edge. When this occurs, the doubling of the integrand that is inherent in equations (22), (25), (27), and (37) is not valid for the entire sample. Let the  $z$ -coordinate of the edge end-point in the negative direction be called  $z_{edge}^-$ , and that in the positive direction be called  $z_{edge}^+$ . If  $z_{edge}^+ < z_0^+$  and  $z_{edge}^- < z_0^-$ , then  $z_{edge}^+$  can be the initial choice for  $z_{range}$ , and the remainder of the contribution to the first sample from the negative side can be calculated with numerical integration of equation (9). If  $z_{edge}^- > z_0^-$  and  $z_{edge}^+ > z_0^+$ , a positive  $z$ -value must be found using the derivation in Appendix A2 which is equivalent to  $z_{edge}^-$  in terms of travel distance, and this value can be the initial choice for  $z_{range}$ . The remainder of the contribution to the first sample from the positive side can be calculated with numerical integration of equation (9). Either of these choices for  $z_{range}$  must also satisfy the requirement of being small compared with  $m_0$  and  $l_0$ .

## 5. Example calculations

This section includes example calculations of edge-diffraction IRs. In each case, the first sample was calculated using an analytical approximation, and the remainder of the IR was calculated with numerical integration. For these results, a sampling frequency of 384 kHz was used unless otherwise stated.

Consider first a wedge as in Figure 5 with  $\theta_W = 270^\circ$ , and the source and receiver placed symmetrically such that  $r_S = 0.2$  m,  $z_S = 0$ ,  $\theta_S = 45^\circ$ ,  $r_R = 1$  m,  $z_R = 0$ , and  $0 < \theta_R < 270^\circ$ . Figure 6 shows the values of  $h_1(n_0)$ ,

<sup>3</sup> With typical sampling rates above 44.1 kHz, the segment contributing to the first sample of the IR will be quite small, and thus this case is by far the more common of the two.

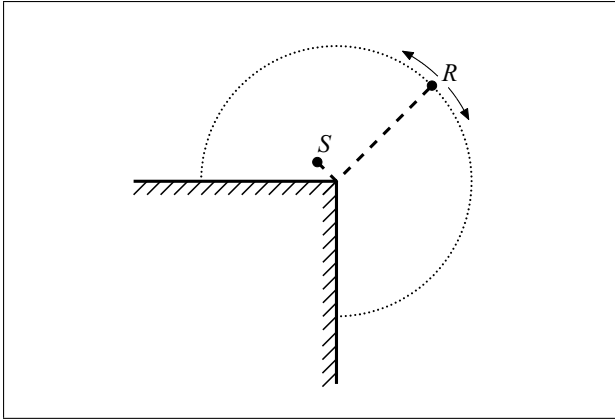


Figure 5. Geometry for a symmetric source and receiver example (shown in 2D), with wedge angle  $\theta_W = 3\pi/2$ . For the source:  $r_S = 0.2$  m,  $z_S = 0$ ,  $\theta_S = \pi/4$ . For the receivers:  $r_R = 1$  m,  $z_R = 0$ ,  $0 < \theta_R < 3\pi/2$ .

Table I. Convergence of  $h_2(n_0)$  to  $-\frac{1}{2R_0}$  near the singularity at  $\theta_R = 225^\circ$  for the geometry shown in Figure 5.

$\theta_R$	Value of $h_2(n_0)$ rel. to $1/R_0$
224.9	-0.478082
224.99	-0.497805
224.999	-0.499780
224.9999	-0.499978
224.99999	-0.499998
224.999999	-0.500000

$h_2(n_0)$ ,  $h_3(n_0)$ , and  $h_4(n_0)$  as function of the receiver angle  $\theta_R$ . Recall that these four values must be summed to give  $h(n_0)$ , the first sample of the diffraction IR. The discontinuity at the shadow boundary is present for  $h_2(n_0)$  at  $\theta_R = 225^\circ$  where  $\phi_2 = \pi + \pi/4 - 5\pi/4 = 0$  and can be seen in Figure 6b. The discontinuity at the specular boundary is present for  $h_4(n_0)$  at  $\theta_R = 135^\circ$  where  $\phi_4 = \pi - \pi/4 - 3\pi/4 = 0$  and can be seen in Figure 6d. For both cases, the value of the singular term can be seen to approach  $\pm \frac{1}{2R_0}$  near the zone boundary as predicted by equation (40). Further results for this example can be seen in Table I, which contains values of  $h_2(n_0)$  for receiver angles approaching the shadow boundary.

Results from an asymmetric case in which  $r_S = 10$  m,  $z_S = 7$  m,  $\theta_S = 45^\circ$ ,  $r_R = 3$  m,  $z_R = 1$  m, and  $0 < \theta_R < 180^\circ$  can be seen in Figure 7. In this example  $\theta_W = 180^\circ$ , simulating an edge between two coplanar surfaces.  $h_1(n_0)$  and  $h_4(n_0)$  are both singular at the specular boundary but with opposite polarities, and thus sum to zero.  $h_2(n_0)$  and  $h_3(n_0)$  also sum to zero, thus giving the expected result of zero amplitude. The singularity at the shadow boundary is not shown because a receiver at the associated angle ( $\theta_R = 225^\circ$ ) would be inside the wedge.

As discussed in section 3.6, the limit value given in equation (40) describes the high-frequency behavior of the diffraction IR at a zone boundary, while the low frequency behavior is also dependent on the edge length and wedge

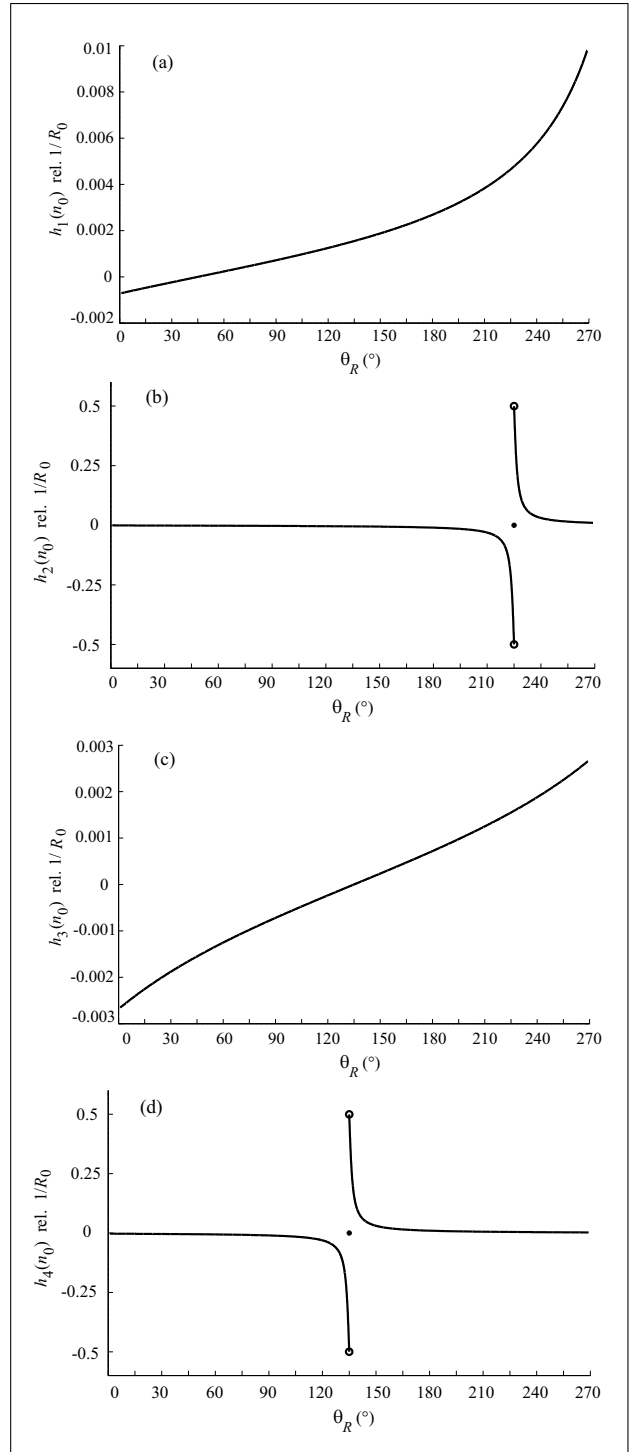


Figure 6. Values of  $h_1(n_0)$ ,  $h_2(n_0)$ ,  $h_3(n_0)$ , and  $h_4(n_0)$  for the geometry shown in Figure 5. Amplitude values are given relative to  $1/R_0$ , and were calculated for  $.001^\circ$  increments of  $\theta_R$ . The discontinuity in  $h_2$  at  $\theta_R = 225^\circ$  is associated with the shadow boundary, and the discontinuity in  $h_4$  at  $\theta_R = 135^\circ$  with the specular boundary. Both approach the limit of  $\pm 1/2R_0$  per equation (40). Note that the y-axis range is not the same for all plots.

angle. An example of the latter dependence can be seen in Figure 8, which contains edge-diffraction impulse responses and the corresponding frequency responses for a 100 m edge with wedge angles ranging from  $195^\circ$  to  $270^\circ$ .

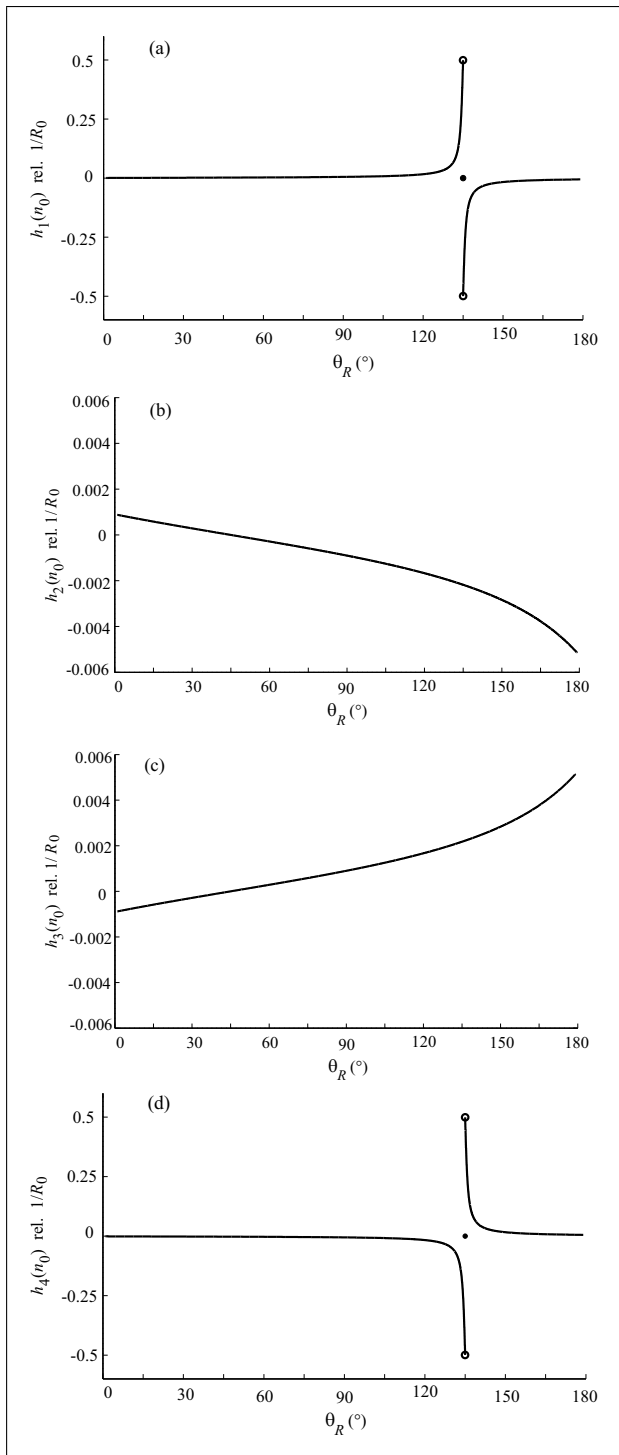


Figure 7. Values of  $h_1(n_0)$ ,  $h_2(n_0)$ ,  $h_3(n_0)$ , and  $h_4(n_0)$  for an edge between two coplanar surfaces ( $\theta_W = 180^\circ$ ), with the source at  $\theta_S = 45^\circ$  and  $0 < \theta_R < 180$ . The singularities in  $h_1(n_0)$  and  $h_4(n_0)$  at  $\theta_R = 135^\circ$  are of opposite polarity and the terms sum to zero.  $h_2(n_0)$  and  $h_3(n_0)$  also sum to zero, thus giving the expected result. Note that the y-axis range is not the same for all plots.

For this example,  $r_S = 2$  m,  $z_S = 0$ ,  $\theta_S = 45^\circ$ ,  $r_R = 30$  m,  $z_R = 0$ ,  $\theta_R = 135.005^\circ$ ,  $f_S = 768$  kHz. The receiver is located 0.005° from the specular boundary (on the “non-illuminated” side) with  $R_0 = 32$  m, and thus equation (40) predicts a flat frequency response at approximately

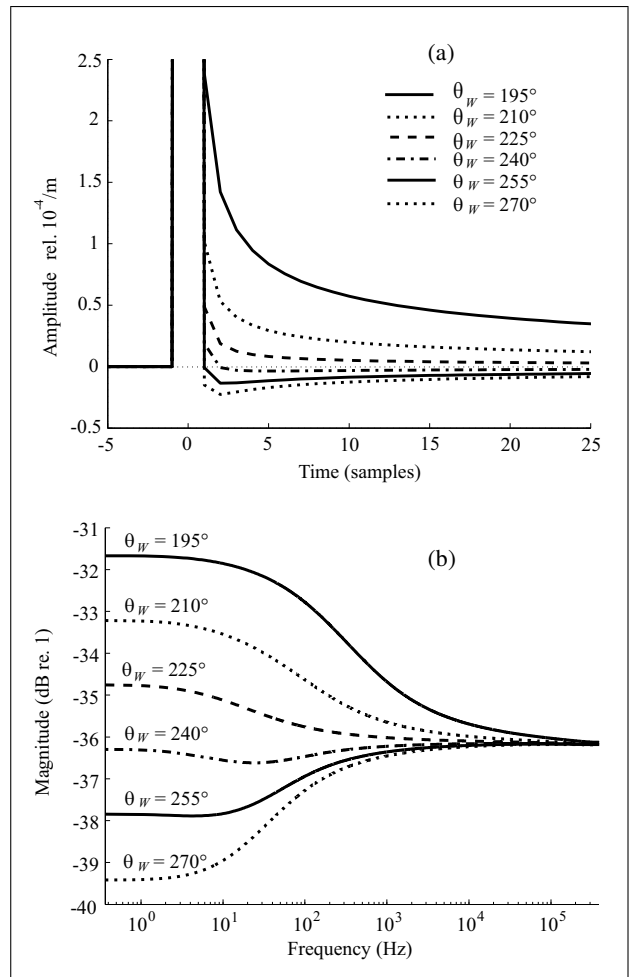


Figure 8. Dependence of edge-diffraction on the wedge angle  $\theta_W$ . (a) A close-up view of the early part of the impulse responses where  $\theta_W$  varies from  $195^\circ$  to  $270^\circ$  in  $15^\circ$  steps. Time has been normalized so that the initial pulses from the apex point of the edge occur at sample 0. The initial-sample amplitudes are all approximately 0.0156. (b) Frequency responses of the impulse responses in (a). Note the consistent high-frequency behavior as predicted by equation (40). For these calculations,  $r_S = 2$  m,  $z_S = 0$ ,  $\theta_S = 45^\circ$ ,  $r_R = 30$  m,  $z_R = 0$ ,  $\theta_R = 135.005^\circ$ ,  $f_S = 768$  kHz, and the edge length is 100 m.

-36.12 dB. The effect of the wedge angle can be seen clearly in both plots. In the time domain, the IRs become more “narrow” as the wedge angle increases, eventually crossing zero ( $\theta_W \geq 240^\circ$ ) and taking negative amplitudes. In the frequency domain, the response at very low frequencies deviates from the limit value by as much as +4.46 dB and -3.30 dB, decreasing monotonically with increasing wedge angle. At high frequencies, there is a small deviation from the expected value, which is an artifact of the limited sampling frequency and the low-pass filtering effect of the integration in equation (9).

## 6. Conclusions

This paper addresses the onset singularity in edge-diffraction impulse responses for receivers at or near specular-

zone and shadow-zone boundaries. Starting with an edge diffraction formulation, based on the BTM solution, in which the diffraction IR is expressed as an integral along the edge, analytical approximations are developed for the integrand along a small section of the edge which includes the apex point. A finite limit value for these approximations has been given, and using this limit it has been shown that the approximations maintain a continuous sound field across zone boundaries when combined with geometrical-acoustics components. The limit value,  $\pm \frac{1}{2R_0}$  where  $R_0$  is the length of the shortest path from the source to the receiver through the edge and the choice of sign is based on the receiver's orientation relative to the boundary, is in agreement with the limit shown to apply to similar conditions with different diffraction models by other authors. The approximations can be coupled with numerical integration for the remainder of the edge to yield the entire edge diffraction IR. Implementation details have been discussed, and sample results given in both the time and frequency domain which show the asymptotic behavior of the approximations. Future work includes extension to higher orders of diffraction, and comparison with measurements of simple geometries where geometrical acoustics and first order diffraction are dominant, e.g. highway noise barriers and orchestra pits.

#### Acknowledgement

This work has been funded in part by a Norwegian Marshall Fund Award from the Norway-America Association, and by the Acoustics Research Centre project from the Research Council of Norway.

## Appendix

### A1. Derivation of the approximations

In order to find an analytical approximation for the integrand  $\beta_i/ml$  in equation (9) around the apex point, serial expansions for the product  $ml$  and for the function  $\cosh(v\eta)$  must be derived. These quantities are first rewritten in terms of the relative  $z$ -coordinate,  $z_{rel}$ , which is defined by equations (10) and (11). Starting with the product  $ml$ , the two terms involved are

$$m = \sqrt{r_S^2 + (z - z_S)^2}, \quad l = \sqrt{r_R^2 + (z - z_R)^2}. \quad (A1)$$

Rewriting in terms of  $z_{rel}$  then yields

$$\begin{aligned} m &= \sqrt{r_S^2 + (z_{rel} + z_a - z_S)^2}, \\ l &= \sqrt{r_R^2 + (z_{rel} + z_a - z_R)^2}. \end{aligned} \quad (A2)$$

Now two constants are introduced,  $m_0$  and  $l_0$ , that denote the distances from the apex point to the source and receiver, respectively,

$$m_0 = \sqrt{r_S^2 + (z_S - z_a)^2}, \quad l_0 = \sqrt{r_R^2 + (z_R - z_a)^2}. \quad (A3)$$

Then  $m$  and  $l$  can be written using  $m_0$  and  $l_0$ ,

$$\begin{aligned} m &= m_0 \sqrt{1 + 2 \frac{z_a - z_S}{m_0} \frac{z_{rel}}{m_0} + \frac{z_{rel}^2}{m_0^2}}, \\ l &= l_0 \sqrt{1 + 2 \frac{z_a - z_R}{l_0} \frac{z_{rel}}{l_0} + \frac{z_{rel}^2}{l_0^2}}. \end{aligned} \quad (A4)$$

By inspecting Figure 4, it can be observed that the quantity  $\cos \psi$  from equation (15) can be written as

$$\cos \psi = \frac{z_R - z_S}{R_0} = \frac{z_a - z_S}{m_0} = \frac{z_R - z_a}{l_0}, \quad (A5)$$

and this quantity can be introduced into equation (A4),

$$\begin{aligned} m &= m_0 \sqrt{1 + 2 \cos \psi \frac{z_{rel}}{m_0} + \frac{z_{rel}^2}{m_0^2}}, \\ l &= l_0 \sqrt{1 - 2 \cos \psi \frac{z_{rel}}{l_0} + \frac{z_{rel}^2}{l_0^2}}. \end{aligned} \quad (A6)$$

For small values of  $z_{rel}/m_0$  and  $z_{rel}/l_0$ , the expressions in equation (A6) can be approximated using a Taylor-series expansion of the square root. Retaining only the terms up to  $z_{rel}^2$  yields

$$\begin{aligned} m &\approx m_0 \left( 1 + \frac{\cos \psi}{m_0} z_{rel} + \frac{\sin^2 \psi}{2m_0^2} z_{rel}^2 \right), \\ l &\approx l_0 \left( 1 - \frac{\cos \psi}{l_0} z_{rel} + \frac{\sin^2 \psi}{2l_0^2} z_{rel}^2 \right). \end{aligned} \quad (A7)$$

The product of these two can be approximated as

$$\begin{aligned} ml &\approx m_0 l_0 + \cos \psi (l_0 - m_0) z_{rel} \\ &+ \frac{\sin^2 \psi}{2} \left( \frac{l_0}{m_0} + \frac{m_0}{l_0} \right) z_{rel}^2 - \cos^2 \psi z_{rel}^2, \end{aligned} \quad (A8)$$

once again keeping only terms only up to second order in  $z_{rel}$ . At this point, the quantity  $\rho$  from equation (14) can be used after inserting it in the expressions for  $m_0$  and  $l_0$ ,

$$\begin{aligned} \frac{m_0}{R_0} &= \frac{r_S}{r_S + r_R} = \frac{1}{1 + \rho}, \\ \frac{l_0}{R_0} &= \frac{r_R}{r_S + r_R} = \frac{\rho}{1 + \rho}. \end{aligned} \quad (A9)$$

Finally, using these expressions for  $m_0$  and  $l_0$  in equation (A8), the product  $ml$  can be rewritten as

$$\begin{aligned} ml &\approx \frac{R_0^2 \rho}{(1 + \rho)^2} + \frac{\cos \psi R_0 (\rho - 1)}{\rho + 1} z_{rel} \\ &+ \frac{\sin^2 \psi}{2} \frac{1 + \rho^2}{\rho} z_{rel}^2 - \cos^2 \psi z_{rel}^2 \\ &= \frac{R_0^2 \rho}{(1 + \rho)^2} + \frac{\cos \psi R_0 (\rho - 1)}{\rho + 1} z_{rel} \\ &+ \frac{\sin^2 \psi (1 + \rho)^2 - 2\rho}{2\rho} z_{rel}^2. \end{aligned} \quad (A10)$$

The second quantity which requires an analytical approximation is  $\cosh(v\eta)$  in equation (4). First, it is written using the alternative formulation,

$$\cosh(v\eta) = \frac{1}{2} [(e^\eta)^v + (e^\eta)^{-v}]. \quad (\text{A11})$$

The quantity  $e^\eta$  can be written

$$e^\eta = y + (y^2 - 1)^{1/2}, \quad (\text{A12})$$

where  $y$  is the auxiliary variable (described in [7])

$$y = \frac{ml + (z - z_S)(z - z_R)}{r_S r_R}. \quad (\text{A13})$$

$y$  can be written in terms of  $z_{rel}$  and then the  $z$ -terms can be rewritten using the  $\rho$ -factor, yielding

$$\begin{aligned} y &= \frac{ml + (z_{rel} + z_a - z_S)(z_{rel} + z_a - z_R)}{r_S r_R} \\ &= \frac{ml}{r_S r_R} - \frac{\rho R_0^2 \cos^2 \psi}{r_S r_R (1 + \rho)^2} \\ &\quad + \frac{R_0(1 - \rho) \cos \psi}{r_S r_R (1 + \rho)} z_{rel} + \frac{z_{rel}^2}{r_S r_R}. \end{aligned} \quad (\text{A14})$$

Introducing the approximation for  $ml$  from equation (A10) and summing the terms yields

$$\begin{aligned} y &\approx 1 + \frac{\sin^2 \psi (1 + \rho)^2}{2\rho r_S r_R} z_{rel}^2 \\ &= 1 + \frac{(1 + \rho)^4}{2\rho^2 R_0^2} z_{rel}^2. \end{aligned} \quad (\text{A15})$$

Since  $y$  is of the form  $1 + \epsilon$  where  $\epsilon$  is a small number, the quantity  $e^\eta$  can be written

$$e^\eta \approx 1 + \epsilon + \sqrt{2\epsilon + \epsilon^2} \approx 1 + \sqrt{2\epsilon} + \epsilon. \quad (\text{A16})$$

The quantity  $\cosh(v\eta)$  is then

$$\cosh(v\eta) = \frac{1}{2} [(1 + \delta)^v + (1 + \delta)^{-v}], \quad (\text{A17})$$

where  $\delta = \sqrt{2\epsilon} + \epsilon$ , and then

$$\begin{aligned} \cosh(v\eta) &\approx \frac{1}{2} \left[ 1 + v\delta - \frac{1}{2}v(1 - v)\delta^2 \right. \\ &\quad \left. + 1 - v\delta + \frac{1}{2}v(1 + v)\delta^2 \right] \\ &= 1 + \frac{1}{2}v^2\delta^2 \approx 1 + v^2\epsilon. \end{aligned} \quad (\text{A18})$$

Finally, inserting the value of  $\epsilon$  from equation (A15) yields expression for  $\cosh(v\eta)$ ,

$$\cosh(v\eta) \approx 1 + v^2 \frac{(1 + \rho)^4}{2\rho^2 R_0^2} z_{rel}^2. \quad (\text{A19})$$

## A2. Calculation of the sample-aligned integration limits $z_{n,1}$ and $z_{n,2}$

As described in section 2.2, the limits of integration  $z_{n,1}$  and  $z_{n,2}$  in equation (9) can be chosen for the  $n$ th sample such that they correspond to the travel times  $(n - 0.5)/f_S$  and  $(n + 0.5)/f_S$ , and thus the diffraction from the resulting edge segment will contribute only to the  $n$ th sample of the impulse response. Let  $D = ct$  be the total travel distance corresponding to time  $t$  from source to receiver through a point on the edge at coordinate  $z_{rel}$  measured relative to the apex point. Then  $D = m + l$  where

$$\begin{aligned} m &= \sqrt{r_S^2 + (z_{rel} - z_{Srel})^2}, \\ l &= \sqrt{r_R^2 + (z_{rel} - z_{Rrel})^2}, \end{aligned} \quad (\text{A20})$$

are the distances from the source to the edge point, and from the edge point to the receiver, respectively.  $z_{Srel} = z_S - z_a$  is the  $z$ -coordinate of the source relative to the apex point, and  $z_{Rrel} = z_R - z_a$  is the  $z$ -coordinate of the receiver relative to the apex point. To find the limits of integration,  $D$  must be set to the desired travel distances  $(c(n \pm 0.5)/f_S)$  and the equation  $D = m + l$  must be solved for  $z_{rel}$ . The quantities  $m_0$  and  $l_0$  from equation (A3) are needed, but in modified form such that

$$m_0 = \sqrt{r_S^2 + z_{Srel}^2}, \quad l_0 = \sqrt{r_R^2 + z_{Rrel}^2}. \quad (\text{A21})$$

Starting with

$$\begin{aligned} D &= \sqrt{r_S^2 + (z_{rel} - z_{Srel})^2} \\ &\quad + \sqrt{r_R^2 + (z_{rel} - z_{Rrel})^2}, \end{aligned} \quad (\text{A22})$$

re-arranging, squaring both sides, and substituting  $m_0$  and  $l_0$  yields

$$z_{rel}^2 - 2z_{rel}z_{Srel} + m_0^2 = \quad (\text{A23})$$

$$D^2 - 2D\sqrt{r_R^2 + (z_{rel} - z_{Rrel})^2} + z_{rel}^2 - 2z_{rel}z_{Rrel} + l_0^2.$$

Further re-arranging yields

$$\begin{aligned} 2z_{rel}(z_{Srel} - z_{Rrel}) - K &= \quad (\text{A24}) \\ 2D\sqrt{r_R^2 + (z_{rel} - z_{Rrel})^2}, \end{aligned}$$

where

$$K = m_0^2 - l_0^2 - D^2. \quad (\text{A25})$$

Squaring both sides yields a quadratic equation in  $z_{rel}$ ,

$$z_{rel}^2 + Bz_{rel} + C = 0, \quad (\text{A26})$$

where

$$B = \frac{2D^2 z_{Rrel} - K(z_{Srel} - z_{Rrel})}{(z_{Srel} - z_{Rrel})^2 - D^2}, \quad (\text{A27})$$

and

$$C = \frac{0.25K^2 - D^2l_0^2}{(z_{Srel} - z_{Rrel})^2 - D^2}, \quad (\text{A28})$$

with solutions

$$z_{rel} = \frac{-B \pm \sqrt{B^2 - 4C}}{2}. \quad (\text{A29})$$

Using this result, setting  $D = c(n-0.5)/f_S$  will result in a value for  $z_{n,1}$ , and setting  $D = c(n+0.5)/f_S$  will result in a value for  $z_{n,2}$  for the  $n$ th sample of the impulse response, choosing either the positive or negative values of  $z_{rel}$ . See Figure 3 for examples of this subdivision for symmetric and asymmetric geometries.

## References

- [1] P. Menounou, J. H. You: Experimental study of the diffracted sound field around jagged edge noise barriers. *J. Acoust. Soc. Am.* **116** (2004) 2843–2854.
- [2] J. Vanderkooy: A simple theory of cabinet edge diffraction. *J. Aud. Eng. Soc.* **39** (1991) 923–933.
- [3] R. R. Torres, U. P. Svensson, M. Kleiner: Computation of edge diffraction for more accurate room acoustics auralization. *J. Acoust. Soc. Am.* **109** (2001) 600–610.
- [4] M. A. Biot, I. Tolstoy: Formulation of wave propagation in infinite media by normal coordinates with an application to diffraction. *J. Acoust. Soc. Am.* **29** (1957) 381–391.
- [5] H. Medwin: Shadowing by finite noise barriers. *J. Acoust. Soc. Am.* **69** (1981) 1060–1064.
- [6] H. Medwin, E. Childs, G. M. Jebsen: Impulse studies of double diffraction: A discrete Huygens interpretation. *J. Acoust. Soc. Am.* **72** (1982) 1005–1013.
- [7] U. P. Svensson, R. I. Fred, J. Vanderkooy: An analytic secondary source model of edge diffraction impulse responses. *J. Acoust. Soc. Am.* **106** (1999) 2331–2344.
- [8] C. S. Clay, W. A. Kinney: Numerical computations of time-domain diffractions from wedges and reflections from facets. *J. Acoust. Soc. Am.* **83** (1988) 2126–2133.
- [9] D. Ouis: Scattering of a spherical wave by a thin hard barrier on a reflecting plane. *Appl. Acoust.* **59** (2000) 19–66.
- [10] U. P. Svensson: Numerical aspects of edge diffraction impulse responses. *Acoust. Sci. & Tech.* **26** (2005) 218–220.
- [11] W. A. Kinney, C. S. Clay, G. A. Sandness: Scattering from a corrugated surface: Comparison between experiment, Helmholtz-Kirchhoff theory, and the facet-ensemble method. *J. Acoust. Soc. Am.* **73** (1983) 183–194.
- [12] D. Ouis: Diffraction by a hard half-plane: Useful approximations to an exact formulation. *J. Sound Vib.* **252** (2002) 191–221.
- [13] S. Li, C. S. Clay: Sound transmission experiments from an impulsive source near rigid wedges. *J. Acoust. Soc. Am.* **84** (1988) 2135–2143.
- [14] P. Calamia, U. P. Svensson: Edge subdivision for fast diffraction calculations. Proc. of the 2005 IEEE Workshop on Applications of Signal Processing to Audio and Acoustics, New Paltz, NY, 2005, 187–190.